Optics Letters

Laguerre–Gaussian modes become elegant after an azimuthal phase modulation

Vasilios Cocotos,[1] Light Mkhumbuza,[1] Kayn A. Forbes,[2] Robert de Mello Koch,[1,3] Angela Dudley,[1,4] and Isaac Nape[1,*]

[1]School of Physics, University of the Witwatersrand, Private Bag 3, Wits Johannesburg 2050, South Africa
[2]School of Chemistry, University of East Anglia, Norwich Research Park, Norwich, Norfolk NR4 7TJ, UK
[3]School of Science, Huzhou University, Huzhou 313000, China
[4]angela.dudley@wits.ac.za
*isaac.nape@wits.ac.za

Received 11 November 2024; revised 12 January 2025; accepted 14 January 2025; posted 15 January 2025; published 7 March 2025

Laguerre–Gaussian (LG) modes are solutions of the paraxial Helmholtz equation in cylindrical coordinates and are associated with light fields carrying orbital angular momentum (OAM). It is customary to modulate such beams using phase-only vortex profiles, e.g. when increasing (laddering up) or decreasing (laddering down) the OAM content of some given LG mode. However, the resulting beams have been shown to be hypergeometric-Gaussian modes, due to the changing radial amplitudes on propagation. In this work, we show that these beams in fact have the angular spectrum of a set of modes known as elegant Laguerre–Gaussian (eLG) modes, which map back to LG-type modes more intuitively than hypergeometric-Gaussian modes. Accordingly, the fields obtain new OAM and radial quantum numbers that depend on the initial OAM and additional OAM gained during modulation.

https://doi.org/10.1364/OL.547825

The standard Laguerre–Gaussian (LG) beam is well-known as an eigenmode of the paraxial wave equation whose mode order is determined by the topological charge $\ell \in \mathbb{Z}$ and radial index $p \in \mathbb{N}_0$. While ℓ tells us the number of intertwined helical wavefronts, and consequently the value of OAM $\ell\hbar$ per photon, the radial index determines the number of nodes, or $p+1$ concentric rings of intensity. Over the past few decades, LG beams have gained significant attention due to their broad applications in areas such as optical trapping and manipulation, classical and quantum optical communications, imaging, metrology, and spectroscopy [1,2]. Popular passive techniques for generating LG beams include spatial light modulators [3], Q-plates [4], and metasurfaces [5]. Active (direct) generation from a source can be achieved in free-space, fiber, and on-chip lasers [1,6].

As extensions of the LG beam, elegant Hermite–Gaussian (eHG) and elegant Laguerre–Gaussian (eLG) beams were introduced in 1973 by Siegman and in 1985 by Takenaka, respectively, as solutions to the paraxial wave equation for free-space propagation [7,8]. The elegance to which these beams owe their namesake arises from the fact that while the LG and HG's polynomial argument is real, the eLG and eHG's polynomial is complex, endowing the mathematics that describes the beams with compactness and elegance, a feature retained even in three-dimensional generalizations (non-paraxial regime) of eLG beams [8,9]. However, before this, eHG and eLG beams had been explored in the context of resonators with variable-reflectivity mirrors [10,11] and lens-like gain media [12,13]. Connections between elegant and standard modes have been established [14], and eLG beams with high radial orders have been shown to share similarities with Bessel–Gaussian (BG) beams [15,16], which are finite-energy realizations of the non-diffracting Bessel beam [17]. eLG beams are also complementary to other complex light fields, even though, due to their complex argument, they display distinctive structural changes in their transverse profiles upon propagation that have been studied in detail [14]. Furthermore, eLG modes exhibit more symmetry compared to LG modes [9,18,19]. Many theoretical studies have also been dedicated to eLG beams pertaining to their vortex structure [20,21], OAM [22,23], and vector wave packet behavior [24].

In this work, we demonstrate that LG beams undergoing azimuthal phase modulation evolve into elegant LG modes upon propagation. It has been previously shown that these types of evolving LG beams can be described as hypergeometric-Gaussian modes [25–27] and, when expressed in the complete LG azimuthal and radial basis, the field represents a superposition of LG modes. However, such a description is unintuitive due to the indices that describe hypergeometric-Gaussian modes. We show here that LG modes undergoing azimuthal phase modulation revert to fields that are characterized by well-defined radial indices and topological charges, specifically the eLG modes.

To begin, let us suppose an LG mode is modulated with a phase profile, $\exp(i\Delta\ell\phi)$, where $\Delta\ell$ is an integer as shown in Figs. 1(a) ($\Delta\ell = 1$) and 1(b) ($\Delta\ell = 2$) and ϕ is the azimuthal coordinate. Initially, the LG mode has the field function $\mathrm{LG}_{\ell_{\mathrm{in}}}(r,\phi) = f_{|\ell_{\mathrm{in}}|}(r)\exp(i\ell_{\mathrm{in}}\phi)$, where ℓ_{in} is the initial topological charge, and $f_{|\ell_{\mathrm{in}}|}(r) = (\sqrt{2}r/w)^{|\ell_{\mathrm{in}}|}\exp\left(-r^2/w^2\right)$ is the radial envelope function for the LG mode, defined in cylindrical coordinates, $(r,\phi,z=0)$. We assume that the initial field does not have radial modes, i.e., initially $p=0$. Here w is the mode size of the embedded Gaussian envelope, where the Gaussian envelope is $\exp(-r^2/w^2)$. An example is illustrated in Fig. 1(a), where

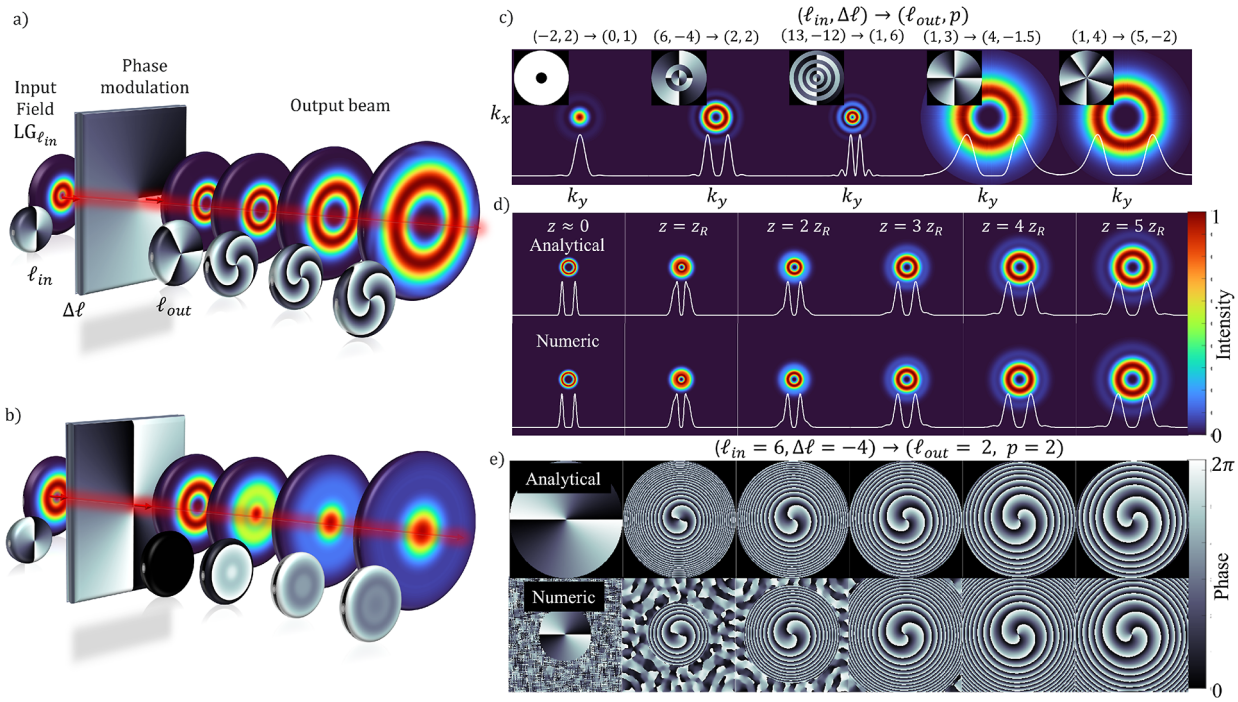

Fig. 1. Concept figure. (a), (b) Conceptual illustration of modulating an LG mode with topological charge ℓ_{in} using a spiral phase ($e^{i\Delta\ell\phi}$) of charge $\Delta\ell$, yielding a new mode with $\ell_{\text{out}} = \ell_{\text{in}} + \Delta\ell$. Shown analytically, for (a) $\ell_{\text{in}} = 2$, $\Delta\ell = 1$ and (b) $\ell_{\text{in}} = -2$, $\Delta\ell = 2$ over distances $z = 0$ to $1.5z_R$ in $0.5z_R$ intervals for intensity and phase profiles. (c) Analytical transverse angular spectral for various $(\ell_{\text{in}}, \Delta\ell)$ producing OAM and radial index pairs, (ℓ_{out}, p), with the intensity profiles and their cross sections in large, and their corresponding phase profiles appearing as insets. (d), (e) Analytical and numerical intensity and phase profiles for $\ell_{\text{in}} = 6$, $\Delta\ell = -4$, resulting in $\ell_{\text{out}} = 2$, $p = 2$.

a beam is numerically propagated for a mode with an initial OAM charge of $\ell_{\text{in}} = 2$. After modulation, the beam acquires an additional OAM charge of $\Delta\ell = 1$, resulting in a final topological charge of $\ell_{\text{out}} = \ell_{\text{in}} + \Delta\ell = 3$. Notably, the beam in this example preserves its characteristic donut-like shape throughout propagation. While the field initially does not have radial modes (nodes), it appears that in some cases, they emerge as the beam propagates, as can be seen in the numerical propagation in Fig. 1(b) for $\ell_{\text{in}} = -2$ and $\Delta\ell = 2$ corresponding to an output OAM topological charge of $\ell_{\text{out}} = 0$. To compute the angular spectrum of the field, we assume Fraunhofer diffraction and exploit the cylindrical symmetry of the modes. Accordingly, the angular spectrum that describes the field can be computed from the Fourier transform:

$$\Psi_{\ell_{\text{out}}}(\mathbf{k}) \propto \mathcal{F}(f_{|\ell_{\text{in}}|}(r)e^{i\ell_{\text{out}}\phi}) = \frac{1}{2\pi}\int f_{|\ell_{\text{in}}|}(r)e^{i\ell_{\text{out}}\phi}e^{i\mathbf{k}\cdot\mathbf{r}}d^2r, \quad \textbf{(1)}$$

mapping from position $\mathbf{r} = (r, \phi)$ to momentum space $\mathbf{k} = (k_r, \phi_k)$, where k_r and ϕ_k are the radial and azimuthal polar coordinates in the momentum space, respectively. By applying the Jacobi–Anger expansion for plane waves and solving the azimuthal and radial integral (that results in the $|\ell_{\text{in}}|$th order Hankel transform of the radial function $f_{|\ell_{\text{in}}|}(r)$), we arrive at the following solution:

$$\Psi_{\ell_{\text{out}},p}(\mathbf{k}) = \mathcal{N}\, i^{-\ell_{\text{out}}}e^{i\ell_{\text{out}}\phi_k}\left(\frac{k_r w}{2}\right)^{|\ell_{\text{out}}|}e^{-(k_r w/2)^2}L_p^{|\ell_{\text{out}}|}\left[\left(\frac{k_r w}{2}\right)^2\right], \quad \textbf{(2)}$$

where $\mathcal{N}$ is a normalization factor and the radial mode index is given by $p = \frac{1}{2}(|\ell_{\text{in}}| - |\ell_{\text{out}}|)$. In the absence of modulation, $p = 0$, and the behavior of the mode reduces to a standard LG mode. To allow for half-integer values for the radial index, we use the generalized Laguerre polynomials defined in terms of the confluent hypergeometric functions, which can be defined as $L_p^{|\ell|}(z) = \frac{(|\ell|+1)_p}{p!}\,{}_1F_1\,(-p; |\ell|+1; z)$, where $(\cdot)_p$ denotes the Pochhammer symbol. This allows the p-index to take negative values as well since it is possible to have $|\ell_{\text{in}}| > |\ell_{\text{out}}|$. The calculated angular spectrum that we have derived resembles that of eLG modes [19], which have the characteristic form, $\text{eLG}_p^m(\rho, \phi_r) = \rho^{|m|}e^{-\rho^2}L_p^{|m|}(\rho^2)e^{im\phi_r}$ for $\rho \equiv \frac{k_r w}{2}$ corresponding to the scaled momentum coordinates, confirming that these fields are indeed from the LG mode family. These modes are orthogonal in the OAM degree of freedom but not in the radial degree of freedom and, nonetheless, form an over-complete set. Figure 1(c) shows exemplary analytical transverse angular spectral intensity profiles for several initial OAM charges (ℓ_{in}) and transferred OAM charge pairs, i.e., $(\ell_{\text{in}}, \Delta\ell)$, that in turn produce the total OAM charges (ℓ_{out}) and radial index (p) pairs, i.e., (ℓ_{out}, p). For the first three cases, we see that the p-index satisfying $p \geq 0$ corresponds to the number of dark rings that can be seen in the intensity profiles of the propagated field. Whereas in the last two cases, corresponding to $p<0$, we see that the field does not have dark rings even though the magnitude of the radial index is nonzero. To appreciate the significance of the radial index, we examine the angular spectrum and, in particular, its polynomial components. For $p \geq 0$, the generalized Laguerre polynomials, expressed using confluent hypergeometric functions, retain a polynomial form, leading to radial profiles with nodes. This is evident in the intensity and phase profiles for $p = 1, 2$, and 6 in Fig. 1(c) (see phase insets). While the intensity does not have p rings, the phase is seen to have $p + 1$ sign changes in the radial direction. That is to say, beginning at the center of the phase profile and moving radially outward, there will be p sudden phase changes. However, for the case where the modes have negative radial indices, shown in the last two examples of Fig. 1(c), the

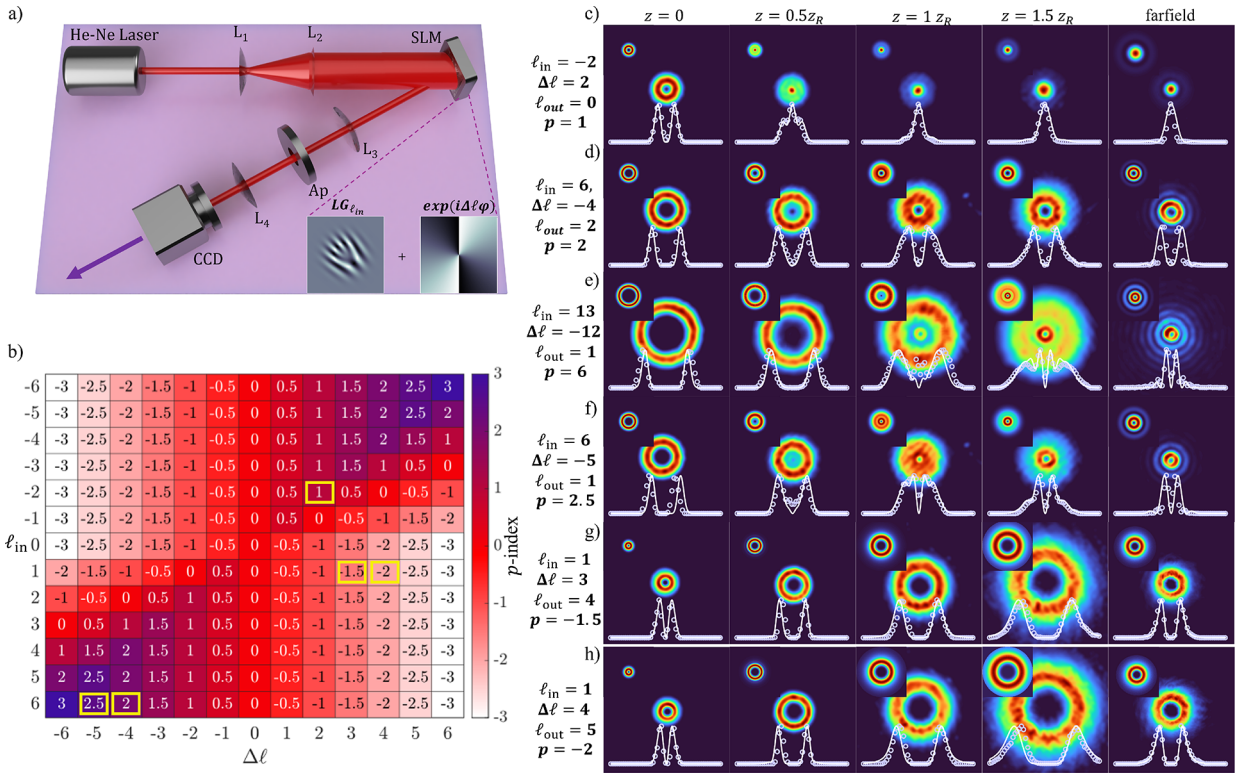

Fig. 2. Experimental figure. (a) Schematic of the experimental setup consisting of an expanded laser beam (using lenses $L_{1(2)}$) that is incident on a spatial light modulator (SLM), with the output mode imaged onto a camera (CCD) (using lenses $L_{3(4)}$). (b) Heatmap of $p-$indexes (or radial index) associated with various choices of ℓ_{in} and $\Delta\ell$. The corresponding radial index is determined by $p = (|\ell_{\text{in}}| - |\ell_{\text{out}}|)/2$. Experimental, theoretical (top, left inset) intensity profiles at propagation distances of $z = 0.0$, $z = 0.5z_R$, $z = z_R$, and $z = 1.5z_R$ and the far-field images for (c) $\ell_{\text{in}} = -2$ and $\Delta\ell = 2$, (d) $\ell_{\text{in}} = 6$ and $\Delta\ell = -4$, (e) $\ell_{\text{in}} = 13$ and $\Delta\ell = -12$, (f) $\ell_{\text{in}} = 6$ and $\Delta\ell = -5$, (g) $\ell_{\text{in}} = 1$ and $\Delta\ell = 3$, and (h) $\ell_{\text{in}} = 1$ and $\Delta\ell = 4$. The cross sections are shown below each measured intensity plot, with the solid line corresponding to the theoretical intensities, whereas the points correspond to the measured values.

modes are defined in terms of convergent series of Laguerre polynomials that have positive radial indices. In this case, two types of solutions are expected; for integer negative values, the functions are still polynomials; however, for non-integer negative values, the functions are infinite series of radial modes [27]. This creates a radial profile resembling an LG mode without nodes ($p = 0$) in the radial direction, despite the nonzero index.

Nonetheless, the radial index we obtain resembles the version derived in Ref. [28], which uses the radial quantum operator and which has states from the LG mode family as its eigenstates. Therefore, this gives us an equation analogous to the principal quantum number, which here can be interpreted as the mode order following, $|\ell_{\text{in}}| = 2p + |\ell_{\text{out}}|$, thereby setting constraints on the allowable radial indexes (p) for a given initial (ℓ_{in}) and output (ℓ_{out}) OAM charge mapping. Moreover, this expression reflects the conservation of the total quanta in the initial field ($|\ell_{\text{in}}|$), suggesting that the transfer of OAM, $\Delta\ell = \ell_{\text{out}} - \ell_{\text{in}}$, is balanced by the introduction of radial modes to compensate for changes in the azimuthal component.

The far-field profile is thus given by the following:

$$\Psi^{\text{Far}}_{\ell_{\text{out}},p}(\mathbf{k}, z) = \frac{\mathcal{N}}{\lambda z} e^{i(kz - \pi/2(\ell_{\text{out}}+1))} e^{i\frac{z}{2k}k_r^2} e^{i\ell_{\text{out}}\phi_k} \times \left(\frac{k_r w}{2}\right)^{|\ell_{\text{out}}|} e^{-(k_r w/2)^2} L_p^{|\ell_{\text{out}}|}\left[\left(\frac{k_r w}{2}\right)^2\right], \tag{3}$$

and can be mapped to spatial coordinates through the expression $k_r = \frac{k}{z}r$, where k is the wavenumber. Further, the far-field expression includes the radial curvature ($e^{i\frac{z}{2k}k_r^2}$), the propagation phase e^{ikz}, and $i^{-\ell_{\text{out}}} = \exp(-i\pi/2\ell_{\text{out}})$), which we interpret to be associated with the Gouy phase in the far field. Accordingly, this result is consistent with the far-field mode function as derived in Ref. [19] (see Eq. (46) in the reference).

To estimate the z-dependent function, we assume that it can be computed from the Fresnel diffraction integral, $\psi_{\ell_{\text{out}}}(\mathbf{r}) \propto \mathcal{F}(f_{|\ell_{\text{in}}|}(r)e^{i\ell_{\text{out}}\phi}e^{i\frac{k}{2z}r^2})$, which is similar to the previous Fourier integral but with the addition of a radially dependent phase modulation factor, $e^{i\frac{k}{2z}r^2}$. Solving this integral in cylindrical coordinates yields the following expression:

$$\Psi_{\ell_{\text{out}},p}(r,\phi,z) = \mathcal{N} e^{i(kz - \pi/2(\ell_{\text{out}}+1))}\left(\frac{q}{w(z)^2}\right)^{1+p+|\ell_{\text{out}}|/2} e^{i\frac{k}{2}\frac{r^2}{R(z)}} \times e^{i\ell_{\text{out}}\phi}\left(\frac{\sqrt{q}r}{w(z)}\right)^{|\ell_{\text{out}}|} e^{-\frac{r^2}{w(z)^2}} L_p^{|\ell_{\text{out}}|}\left[\frac{qr^2}{w(z)^2}\right], \tag{4}$$

where $w(z) = w_0\sqrt{1 + \left(\frac{z}{z_R}\right)^2}$, $q = 1 + i\frac{z_R}{z}$, $R(z) = (z^2 + z_R^2)/z$ is the radius of curvature and $z_R = 1/2kw^2$ is the Rayleigh range of the embedded Gaussian mode from the initial beam $\text{LG}_{\ell_{\text{in}}}(\cdot)$. Exemplary z-dependent intensity (Fig. 1(d)) and phase (Fig. 1(e)) profiles are shown using our analytical formulas in Eq. (4) (top panel) and the numerically propagated simulations

(bottom panel) using the angular spectrum propagation method. The analytical and numerical results are in perfect agreement producing a fidelity of 100% in each case. The experiment validating our theory is shown in Fig. 2(a). A He–Ne laser beam ($\lambda = 633$ nm) passed through a lens system ($L_{1(2)}$) to ensure uniform intensity on a phase-only spatial light modulator (SLM). The SLM was encoded with a complex amplitude hologram of an LG mode (OAM ℓ_{in}, $p = 0$) multiplied by an additional azimuthal phase $\exp(\text{i}\Delta\ell)$ (inset, Fig. 2(a)). A 4f imaging system (L_3 and L_4) enabled spatial filtering of the first diffraction order and imaging of the generated field on a Thorlabs CCD camera, which captured intensity profiles from the image plane to 1.5 times the Rayleigh range and the far field. The combinations selected for ℓ_{in} and $\Delta\ell$ are highlighted (by yellow outlines) in the table of Fig. 2(b), except for the case of Fig. 2(e), which falls outside the plotted range of the heatmap. The intensity profiles obtained are presented in Figs. 2(c)–2(h), where an initial OAM mode of ℓ_{in} is produced and then modulated with an azimuthal phase of $\Delta\ell$. The value of $\Delta\ell$ is theoretically limited to any integer but may be practically constrained by factors such as the diffraction limit and aperture size used to record the intensity profile. Here the first three measurements, i.e., Figs. 2(c)–2(e), include cases for (ℓ_{out}, p) corresponding to (0, 1), (2, 2), and (1, 6), which were produced from pairs $(\ell_{\text{in}}, \Delta\ell)$ of (−2, 2), (6, −4), and (13, −12), respectively. These cases were chosen as they all produce positive radial indices. Next we show a result for a case where the radial index is a half-integer value, shown in Fig. 2(f) for $(\ell_{\text{out}}, p) = (1, 2.5)$, which was produced by $(\ell_{\text{in}}, \Delta\ell) = (6, -5)$. While the cases shown so far correspond to positive integer values for the radial index (p), since $p = \frac{1}{2}(|\ell_{\text{in}}| - |\ell_{\text{out}}|)$, the p-index can be negative in value. We show measurements for such cases in Figs. 2(g) and 2(h) for $p = -1.5$ and $p = -2$, for half-integer and integer cases, with corresponding topological charges of $\ell_{\text{out}} = 4$ and $\ell_{\text{out}} = 5$, respectively. These were produced for $(\ell_{\text{in}}, \Delta\ell)$ pairs corresponding to (1, 3) and (1, 4) for Figs. 2(g) and 2(h), respectively. To measure the accuracy of the experimental results, a correlation between the experimental intensity profiles and the theoretical (top, left inset) intensity profiles was performed for each of these mentioned cases. Each case produced correlations of above 90%, showing a clear agreement, as can be confirmed by cross-sectional plots of the analytical (solid lines) and experimental results (points).

To conclude, we have examined the behavior of LG modes modulated by an azimuthal phase factor and observed that the resultant modes have the angular spectrum of eLG beams, made apparent by their matching intensity profiles. Previously, it was deduced that modulation of LG modes with a phase-only spiral phase was deleterious as it reduced mode purity and beam power [27]; however, here we have shown that these modes have an analytical expression that can be interpreted again in terms of LG mode families (though it has been shown that they are also hypergeometric-Gaussian mode functions [26]). The link to eLG modes opens up the possibility of controlling the radial index via phase-only control of the OAM content of an optical field; this unveils a coupling between the radial and azimuthal degrees of freedom. We emphasize that while the p-modes generated by these eLG fields are not orthogonal in the p-mode index, their ability to assume negative values is intriguing, as it arises from the conservation of the mode number. A detailed interpretation of this phenomenon will be explored in future studies.

Funding. Optica (University of Witwatersrand Emerging Leader in Quantum Optics Chair); South African Quantum Initiative (SAQuTI); DSI Rentalpool Programme.

Acknowledgment. The authors acknowledge financial support from the South African Quantum Initiative (SAQuTI) and the DSI Rentalpool programme. The research of RdMK is supported by a start up research fund of Huzhou University, a Zhejiang Province talent award, and by a Changjiang Scholar award.

Disclosures. IN: Optica (F).

Data availability. Data underlying the results presented in this paper are not publicly available at this time but may be obtained from the authors upon reasonable request.

REFERENCES

1. Y. Shen, X. Wang, Z. Xie, *et al.*, Light: Sci. Appl. **8**, 90 (2019).
2. Y. Yang, Y.-X. Ren, M. Chen, *et al.*, Adv. Photonics **3**, 034001 (2021).
3. A. Forbes, A. Dudley, and M. McLaren, Adv. Opt. Photonics **8**, 200 (2016).
4. A. Rubano, F. Cardano, B. Piccirillo, *et al.*, J. Opt. Soc. Am. B **36**, D70 (2019).
5. H. Ahmed, H. Kim, Y. Zhang, *et al.*, Nanophotonics **11**, 941 (2022).
6. A. Forbes, L. Mkhumbuza, and L. Feng, Nat. Rev. Phys. **6**, 352 (2024).
7. A. E. Siegman, J. Opt. Soc. Am. **63**, 1093 (1973).
8. T. Takenaka, M. Yokota, and O. Fukumitsu, J. Opt. Soc. Am. A **2**, 826 (1985).
9. E. Zauderer, J. Opt. Soc. Am. A **3**, 465 (1986).
10. N. Vakhimov, Radio Eng. Electron. Phys. (USSR) **10**, 1439 (1965).
11. H. Zucker, Bell Syst. Tech. J. **49**, 2349 (1970).
12. J. Arnaud, J. Opt. Soc. Am. **61**, 751 (1971).
13. L. W. Casperson, J. Opt. Soc. Am. **66**, 1373 (1976).
14. M. Yokota, T. Takenaka, and O. Fukumitsu, Trans. Inst. Electron. Commun. Eng. Jpn. **68-C**, 1130 (1985).
15. C. Sheppard and T. Wilson, IEE J. Microwaves, Opt. Acoust. **2**, 105 (1978).
16. F. Gori, G. Guattari, and C. Padovani, Opt. Commun. **64**, 491 (1987).
17. J. Durnin and J. Miceli Jr, Opt. News **13**, 27 (1987).
18. S. Saghafi and C. Sheppard, Opt. Commun. **153**, 207 (1998).
19. S. Saghafi and C. Sheppard, J. Mod. Opt. **45**, 1999 (1998).
20. I. Martinez-Castellanos and J. C. Gutiérrez-Vega, J. Opt. Soc. Am. A **30**, 2395 (2013).
21. W. Nasalski, Appl. Phys. B **115**, 155 (2014).
22. D. Lopez-Mago, J. Davila-Rodriguez, and J. C. Gutiérrez-Vega, J. Opt. **15**, 125709 (2013).
23. V. Kotlyar and A. Kovalev, J. Opt. Soc. Am. A **31**, 274 (2014).
24. W. Nasalski, Opt. Lett. **38**, 809 (2013).
25. V. Kotlyar, R. Skidanov, S. Khonina, *et al.*, Opt. Lett. **32**, 742 (2007).
26. E. Karimi, G. Zito, B. Piccirillo, *et al.*, Opt. Lett. **32**, 3053 (2007).
27. B. Sephton, A. Dudley, and A. Forbes, Appl. Opt. **55**, 7830 (2016).
28. E. Karimi, R. Boyd, P. De La Hoz, *et al.*, Phys. Rev. A **89**, 063813 (2014).